Article

Chitosan-Carboxymethylcellulose Hydrogels as Electrolytes for Zinc–Air Batteries: An Approach to the Transition towards Renewable Energy Storage Devices

María Fernanda Bósquez-Cáceres [1], Lola De Lima [1], Vivian Morera Córdova [1], Anabel D. Delgado [2], José Béjar [2], Noé Arjona [3], Lorena Álvarez-Contreras [2,*] and Juan P. Tafur [1,*]

1   Grupo de Investigación Aplicada en Materiales y Procesos (GIAMP), School of Chemical Sciences & Engineering, Yachay Tech University, Urcuquí 100115, Ecuador
2   Centro de Investigación en Materiales Avanzados S.C. (CIMAV), Miguel de Cervantes No. 120, Complejo Industrial Chihuahua, Chihuahua 31136, Mexico
3   Centro de Investigación y Desarrollo Tecnológico en Electroquímica S.C., Pedro Escobedo, Querétaro 76703, Mexico
*   Correspondence: lorena.alvarez@cimav.edu.mx (L.Á.-C.); jtafur@yachaytech.edu.ec (J.P.T.)

Abstract: Biopolymers are promising materials as electrolytes with high flexibility, good performance, cost effectiveness, high compatibility with solvents, and film-forming ability. Chitosan (CS) and carboxymethylcellulose (CMC) can form an intermolecular complex, giving rise to hydrogels capable of absorbing ionic solutions. Citric acid (CA) is an effective biological chemical crosslinker that assists the formation of amide and ester bonds between CMC and CS, resulting in a structure with high ionic conductivity and good structural integrity. In this study, a chemical crosslinking strategy is used to synthesize electrolyte hydrogels for zinc–air batteries. The effects of crosslinking are studied on the structural and electrochemical performance of the membranes. The results show an improvement in the ionic conductivity with respect to the homologous electrolyte hydrogel systems reported, with a maximum of 0.19 S·cm^{-1} at 30 °C. In addition, the cyclic voltammetry studies showed a current intensity increase at higher CA content, reaching values of 360 mA·cm^{-2}. Structural characterization suggests a higher thermal stability and a decrease in the degree of crystallinity caused by the polymers' crosslinking. Finally, these membranes were tested in Zn–air batteries, obtaining power densities of 85 mW·cm^{-2}. The proposed hydrogels show to be appropriate for energy zinc–air battery applications and present an alternative to support the sustainable energy transition.

Keywords: zinc–air batteries; electrolytes; hydrogels; biopolymers; crosslinking; casting technique

1. Introduction

To mitigate environmental problems, a transition to clean energy sources is essential, such as wind and solar, which have the limitation of being intermittent. An attractive alternative is the development of sustainable rechargeable batteries for renewable energy storage, such as metal–air batteries. In aqueous metal–air batteries, zinc as an anode presents strategic characteristics for battery performance, such as a high volumetric capacity, low redox potential (−0.76 V vs. standard hydrogen electrode), and lower reactivity. It is a chemical element of high abundance, and its use lowers the battery manufacturing cost and toxicity, and it has good safety [1–8]. These characteristics make it an appropriate element to develop ecofriendly batteries. In addition, zinc–air batteries (ZABs) are of great research interest, since they are characterized by the electrochemical coupling of a negative metal electrode to an air-breathing positive electrode, with high theoretical energy densities, even 10 times higher than their lithium ion counterparts [9–11].

A key feature in the design of new batteries is the physical state of the electrolyte. Most commercial batteries use liquid electrolytes. These batteries present safety, toxicity,

flammability, and leakage problems [12–14]. On the other hand, the growth of dendrites on the metal electrode and the corrosion that occurs at the interfaces reduce the capacity and life cycle of the battery and can even generate unequal currents during charging and preferential nucleation, causing fires [15–20]. This is why great attention is currently devoted to the development of solid or gel electrolytes.

Polymer electrolytes (PEs) have very attractive characteristics. They are flexible and have good performance [21–24]. Mo et al. [25] proposed a polymer electrolyte for flexible Zn batteries. The proposal of these authors demonstrated that PEs are an effective solution to avoid dendrite penetration, hydrogen evolution reaction, and corrosion. However, the main problems of these materials are their low battery efficiencies from poor ionic conductivities, low electrochemical stabilities, insufficient mechanical strength, and huge interfacial resistance [26,27].

Chitosan (CS) is an alternative for electrochemical applications, because it is an ecofriendly and biopolymeric material that is nontoxic, biodegradable, and a good hydrogel former [28]. Its molecular structure presents lone electron pairs at the oxygen atom from hydroxyl and a nitrogen atom from amino groups, making it an appropriate polymer host for ionic conduction. Due to the fact of these characteristics, hydrogels, membranes/films, fiber, and sponges formed of chitosan biomaterial have been reported for numerous biotechnology, medicine engineering, environmental, and industrial applications [29,30]. CS has been used to form blends with carboxymethylcellulose (CMC), a biopolymer that forms intermacromolecular complexes through strong electrostatic and hydrogen bonding interactions with CS [31,32]. Bakar et al. [33] reported that the highest ionic conductivity achieved by solid CMC-CS PEs doped with dodecyl trimethyl ammonium bromide was 1.82×10^{-6} S/cm. This result was improved by Rani et al. [34] to 1.03×10^{-5} S cm^{-1} by adding ammonium nitrate to the polymer blend.

Biopolymer hydrogels solve many of the drawbacks of other types of electrolytes. They have better ductility and flexibility, adapt to various working environments because of their self-healing ability, exhibit shape memory, and have the ability to stretch their crosslinked network of polymer chains with fluid-filled interstitial spaces [35,36]. CMC-CS hydrogels can be synthesized by chemical crosslinking. There is scientific evidence for the use of glutaraldehyde [32], arginine [37], sodium alginate [38], fumaric acid, and tartaric acid [39] as crosslinking agents. In particular, citric acid (CA) is an effective chemical crosslinker that leads to the formation of amide and ester bonds between CMC and CS, generating a structure with porous networks and good mechanical stability [40].

KOH is an ionic salt used as an ion source to improve the ionic conductivity of the system [41,42]. Iles et al. [43] achieved a maximum ionic conductivity of 0.019 S cm^{-1} with a polymer gel electrolyte composed of polyvinyl alcohol (PVA) and a terpolymer composed of butyl acrylate, vinyl acetate, and vinyl neodecanoate (VAVTD) and a KOH solution. In this work, hydrogels were synthesized from CS and CMC with the addition of CA to form the host matrix doped with a concentrated 12 M KOH solution. The structural, thermal, and electrochemical properties of the synthesized membranes were analyzed as a function of the crosslinker addition and ratios. The results indicate that it is a good material to be applied as hydrogel electrolytes in Zn–air batteries.

2. Materials and Methods

Chitosan food grade (90.6% deacetylated [44]) (purity 100%, BioFitnest), carboxymethyl cellulose sodium salt (sodium glycolate max. 0.4%, high viscosity grade), and citric acid anhydrous (purity 99.5%) were acquired from Loba Chemie. Acetic acid glacial anhydrous for the analysis (purity 100%) and KOH pellets anhydrous (purity $\geq$ 99.95%) were acquired from Sigma Aldrich. The reagents were used directly for electrolyte membrane preparation. Distilled water was used as a solvent in the polymer blending.

The Zn discs (99.999%) and Pt plates (99.97%) used in these cells were purchased from Goodfellow. Hydrogel electrolytes were sandwiches between Zn and Pt electrodes

(Zn/Hydrogel/Pt cell) or two Zn discs (Zn/hydrogel/Zn cell) (Beit Shemesh, Israel) and Al_2O_3 polishing suspension (1 and 0.05 micron), Buehler (Lake Bluff, IL, USA).

2.1. Preparation of the CMC-CS and CMC-CS-CA Hydrogels

The hydrogels were synthesized using the solution polymerization/crosslinking methods reported by Calderon et al., with some modifications [44]. The hydrogel components were prepared separately; 2 g of CS was dissolved in 100 mL of 1% (v/v) acetic acid solution, 2 g of CMC in 100 mL of distilled water, and 4 g of CA in 100 mL of distilled water. The polymer solutions were stirred overnight until homogeneous solutions were obtained. Subsequently, the hydrogels were synthesized in a 3:1 CMC/CS volume ratio, varying the amounts of CA added (Table 1). A membrane without CA was prepared to contrast the results of the crosslinker effect. The different mixtures were prepared using an immersion mixer for 3 min. Then, the mixtures were sonicated at 40 kHz at 60 °C for 60 min. The hydrogels were dried in an oven at 80 °C for 60 min. The excess liquid was removed to proceed to drying under a fume hood for over a week. The resulting membranes were stored in a desiccator for further characterization in a dry form. In parallel, another set of hydrogels was immersed in a 12 M KOH solution for 48 h before being subjected to the different characterization techniques. To label the latter as hydrogels, "sw" was added to the hydrogel codes (Table 1).

Table 1. Codes to name the hydrogel polymer electrolytes used in this work.

Electrolyte	Hydrogel Code
CMC90/CS30	CMC-CS
CMC90/CS30/CA30	CA30
CMC90/CS30/CA40	CA40
CMC90/CS30/CA50	CA50
CMC90/CS30 "sw"	CMC-CS sw
CMC90/CS30/CA30 "sw"	CA30 sw
CMC90/CS30/CA40 "sw"	CA40 sw
CMC90/CS30/CA50 "sw"	CA50 sw

2.2. Swelling Behavior of the Hydrogels

The hydrogels were weighed before the hydration in 12 M KOH and after 48 h of being immersed. For calculation, the swelling ratio (SR) shown in Equation (1) was used.

$$SR = \frac{W_T - W_0}{W_0} \times 100\% \tag{1}$$

where W is weight or volume, and the subindexes $_T$ and $_0$ represent the swollen hydrogel and the initial hydrogel, respectively.

2.3. Structural, Thermal, and Electrochemical Characterization
2.3.1. ATR-FTIR Methods

To analyze the specific functional groups of the CMC and CS polymers and the developed composite hydrogels, FT-infrared spectroscopy (FTIR) was conducted in the solid state by attenuated total reflectance (ATR) using a spectrophotometer (Cary 630, Agilent Technologies Inc., Santa Clara, CA, USA) equipped with a 1-bounce diamond ATR accessory. The spectra were registered in the range of 4000–400 cm^{-1}, with a resolution of 4 cm^{-1}, and 64 scans were performed.

2.3.2. XRD Characterization

X-ray diffraction (XRD) patterns were recorded using a computer-controlled Rigaku Mini-flex-600 with a D/tex Ultra 2 detector 26 (Rigaku, Tokyo, Japan). The measurement conditions were 40 kV and 15 mA for the X-ray generator in a sealed tube with a Ni-filtered Cu Kα radiation source (λ = 0.15418 nm). For data collection, the membranes were placed

in a sample holder, and the angular region selected was 2θ = 5°–80° with a step width of 0.01°. Match! Software (Crystal Impact, Bonn, Germany) was used to quantify the degree of crystallinity of each membrane [45].

2.3.3. SEM and BET Characterization

In order to study the hydrogels' morphology, field–emission scanning electron microscopy was used (FE–SEM, JEOL JSM–7401F microscope, JEOL Ltd., Tokyo, Japan). A Brunauer–Emmett–Teller (BET) analysis was performed using N_2 adsorption/desorption isotherms at −195 °C employing a S–BET Autosorb iQ2 (Quantachrome Instruments, Boynton Beach, FL, USA). Before the adsorption/desorption test, each membrane was treated at 80 °C in a vacuum for 1 h.

2.3.4. Thermal Analysis

The thermal properties of hydrogels were studied by thermogravimetric analysis (TGA) and differential scanning calorimetry (DSC) using a DSC-TGA Q600 (TA Instruments, New Castle, DE, USA). Nitrogen was employed as the purge gas. The temperature range used was from 25 to 800 °C with a heating rate of 10 °C min^{-1}.

2.3.5. Electrochemical Measurements

To evaluate the electrochemical behavior of the hydrogels, potential electrochemical impedance spectroscopy (PEIS) was performed using a VIONIC instrument (Metrohm model, Ecuador). The frequency range for the PEIS varied from 100 kHz to 1 Hz, and the cell configuration used was Pt/hydrogel/Pt, with a 1 cm^2 area Pt blocking the electrodes. The conductivity at different temperatures was examined in the range of 0 to 60 °C with ±1 °C precision using a Julabo circulator Polyscience (−40 °C, 15 L). Four measurements were performed for each hydrogel and temperature. The system was stabilized after each temperature drop for 5 min before taking the resistance measurement. The ionic conductivity (σ) was calculated using Equation (2):

$$\sigma = \frac{l}{A \times R_b} \tag{2}$$

where l is the film thickness, A is the Pt electrode area, and R_b is the bulk resistance obtained from the intersections of the impedance curve with the *x*-axis. Four impedance measurements were carried out for each membrane. To determine the activation energy (E_a) of each electrolyte, the Arrhenius Equation (3) was used with a linear fitting by plotting a logarithmic relationship between ln(σ) and 1000/T:

$$\sigma = \sigma_0 \exp\left(-\frac{E_a}{K_b \times (T)}\right) \tag{3}$$

where K_b is the Boltzmann's constant, T is the absolute temperature, and σ_0 is a pre-exponential factor [46].

The linear sweep voltammetry (LSV) staircase of the hydrogels was registered between 0.0 and +4.0 V using a Zn/hydrogel/Pt cell. Pt was used as the working electrode, and a Zn disc served both as the counter electrode and the reference electrode. The measurements were performed at a speed of 1 mV/s. Cyclic voltammetry (CV) was performed to evaluate the electrochemical behavior of the hydrogels. The CV studies were carried out using a Zn/hydrogel/Zn symmetric two-electrode cell with Zn electrodes of 0.5 cm^2 and a scanning speed of 50 mV·s^{-1} in a symmetric potential window from −1.5 to +1.5 V.

2.4. Battery Tests

The battery tests were conducted in an AMETEK® VersaSTAT 3 potentiostat/galvanostat (Princeton Applied Research, Berwyn, IL, USA). The anode consisted of a piece of polished high-purity Zn foil (15 × 10 mm length and width, 0.2 mm in depth, purity 99.9%, Yun-

express Inc., Shenzhen, China). SIGRACET® 39 B slides (15×10 mm length and width, 0.4 mm in depth) impregnated with commercial catalytic ink and Pt/C (20% wt.%) were used as a cathode. The catalyst mass loading was 1 mg cm^{-2}. For the battery assembly, the hydrogels were placed between the two electrodes. The discharge current density was -3 mA cm^{-2}, and the cut-off voltage was 0.2 V. The specific capacitance was determined through the zinc weight loss after discharging the Zn–air battery at 1.98 mA cm^{-2}.

3. Results

### 3.1. Formation Reaction of the Hydrogels

The CMC in an anionic polyelectrolyte form reacts with chitosan (cationic polyelectrolyte) by ionic interactions/crosslinking to form CMC–CS [47], leading to intra- and intercharge compensation (Figure 1a). However, with the introduction of CA, in addition to the ionic interaction, there is a reaction of esterification [48] because of the –OH and –COOH groups added to the system, resulting in the formation of hydrogels (Figure 1b). The primary –OH group of the carboxylic acid present in CA is known to be more reactive than the –OH group formed in the CMC-CS uncrosslinked membrane, assuring the esterification reaction with the CA. The crosslinking reaction seeks to increase the number of –OH and –COOH, functional groups desired in a polymer host for ionic conduction systems.
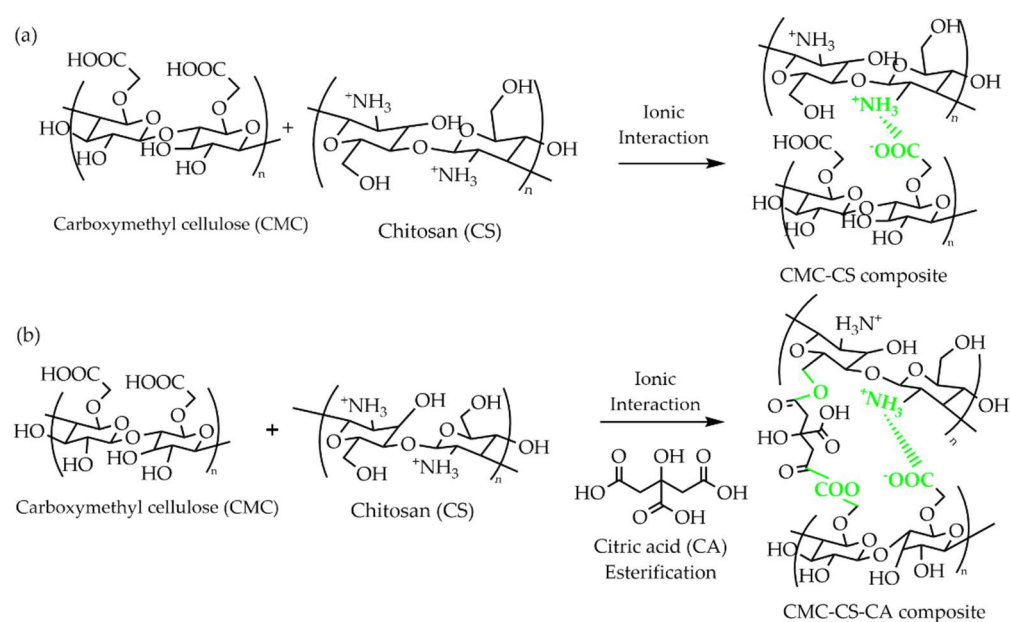
Figure 1. Proposed reaction for the formation of the (**a**) CMC–CS and (**b**) CMC-CS-CA hydrogels.

3.2. Swelling Behavior

The SR of the soaked membranes was calculated, using Equation (1), by the KOH uptake in the hydrogels (Figure 2). It was observed that the noncrosslinked membrane exhibited the highest KOH uptake and volume change (288.68 ± 26.49 wt.%, 37.5 vol.%). In the case of the crosslinked hydrogels, a decrease in the SR was observed as the proportion of CA increased. This behavior agrees with that reported by Fekete et al. [49], who noticed a lower degree of swelling when a higher crosslink density was achieved. However, it is noteworthy that the CA50 membrane, which swelled the least, absorbed approximately 1.5 times its weight with a very low volume change (Figure 2) pointing to a higher swelling capacity in contrast to other polymeric blends [50,51]. In the synthesized hydrogels, the KOH plays the role of an electrolyte ionic species donor to increase the ionic conductivity of the system. In addition, it has been reported that KOH is able to enter the polymer backbone causing conformational changes [52]. Additionally, the thickness of the hydrogels ranged between 0.28 and 0.36 cm (Table S1).
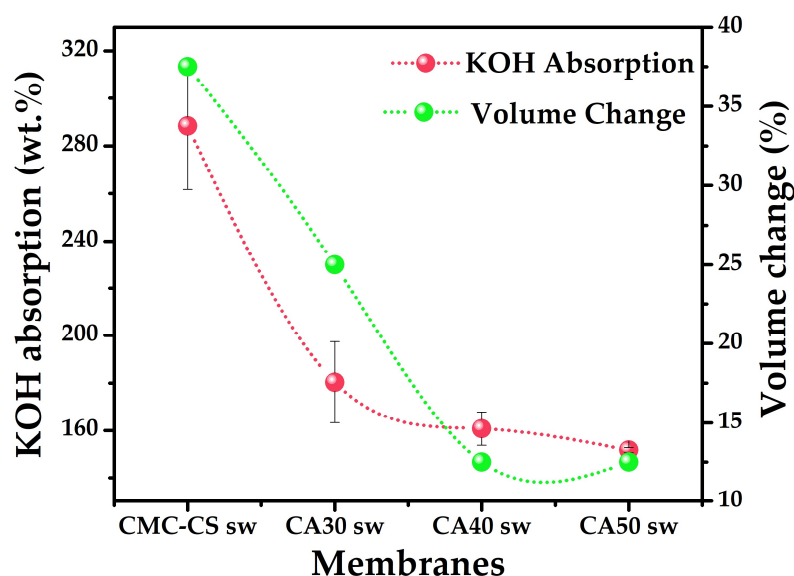
Figure 2. Swelling behavior in mass percentage and volume change of the CMC-CS sw hydrogels at different CA proportions.

3.3. Structural Characterization

3.3.1. ATR-FTIR Analysis

The ATR-FTIR spectral data (Figure 3a) of the CS and CMC polymers showed typical spectral bands. For the pure CS film, the spectrum showed a band in the region between 3100 and 3500 cm^{-1}, assigned to the –OH/NH stretching vibrations [53]. The band at 2920 cm^{-1} corresponded to the C–H bond of the methylene group attached to the primary alcohol. In addition, two peaks observed at 2869 and 2857 cm^{-1} were related to the asymmetric and symmetric C–H stretching vibration of the N–acetyl group. The band at 1610 cm^{-1} was related to the carbonyl assigned to the stretching vibrations of the acetylated amino groups (amide I) and 1541 cm^{-1} for the N–H bending vibration of the primary amine (amide II), as reported previously [54]. The bands of the glycosidic bonds of the skeletal polysaccharides at 1150 and 1063 cm^{-1} were again related to the stretching of the asymmetric C–O bridge, while the peak at 1016 cm^{-1} was assigned to the vibration of the C–O–C pyranose ring and the β–glycosidic bond, giving rise to bands similar to those reported by Corazzari et al. [55]. In the spectrum obtained for the pure CMC film, a fundamental band at 3209 cm^{-1}, attributable to the –OH stretching vibration, was observed. On the other hand, there was a band at 1585 cm^{-1} assigned to the symmetric stretching vibration of the carbonyl [56]. The bands observed at 1425 and 1375 cm^{-1} were assigned to the –CH_2 stretching and –OH bending vibration of the CMC [57], while those at 1114 and 1024 cm^{-1} were characteristic of the C–O stretching of the polysaccharide backbone [58].

In the case of the CMC-CS membrane, along with the fundamental bands that are characteristic for both polymers, a band at 1578 cm^{-1} was observed, which was associated with the symmetric stretching vibrations of the COO– groups for the CMC (1584 cm^{-1}) and to the N–H bending vibration (1563 cm^{-1}) of the –NH_2 groups in chitosan. However, this band has shifted to 1578 cm^{-1}, suggesting ionic interactions and/or hydrogen bonds between the CS and the CMC [59]. There is evidence that hydrogen bridge bonds between the chitosan and the CMC could also be a factor in this shift [39]. The band shift to low/high wavenumbers either weakened/strengthened, indicating crosslinking and the extent of the linkage between the biopolymer backbone and the crosslinker [60].

As for the CA30, CA40, and CA50 spectra, there is evidence pointing to the formation of ester bonds due to the fact of CA insertion, with the peak located at 1717 cm^{-1}, where the difference in the peak intensity between the three hydrogels was given by the degree of chemical crosslinking [39]. In the pure polymers and in the membrane without CA, this peak was absent. In addition, the peak at 1578 cm^{-1} was also present in the crosslinked

membranes. This allows us to conclude that both physical interactions and chemical bonds occurred.
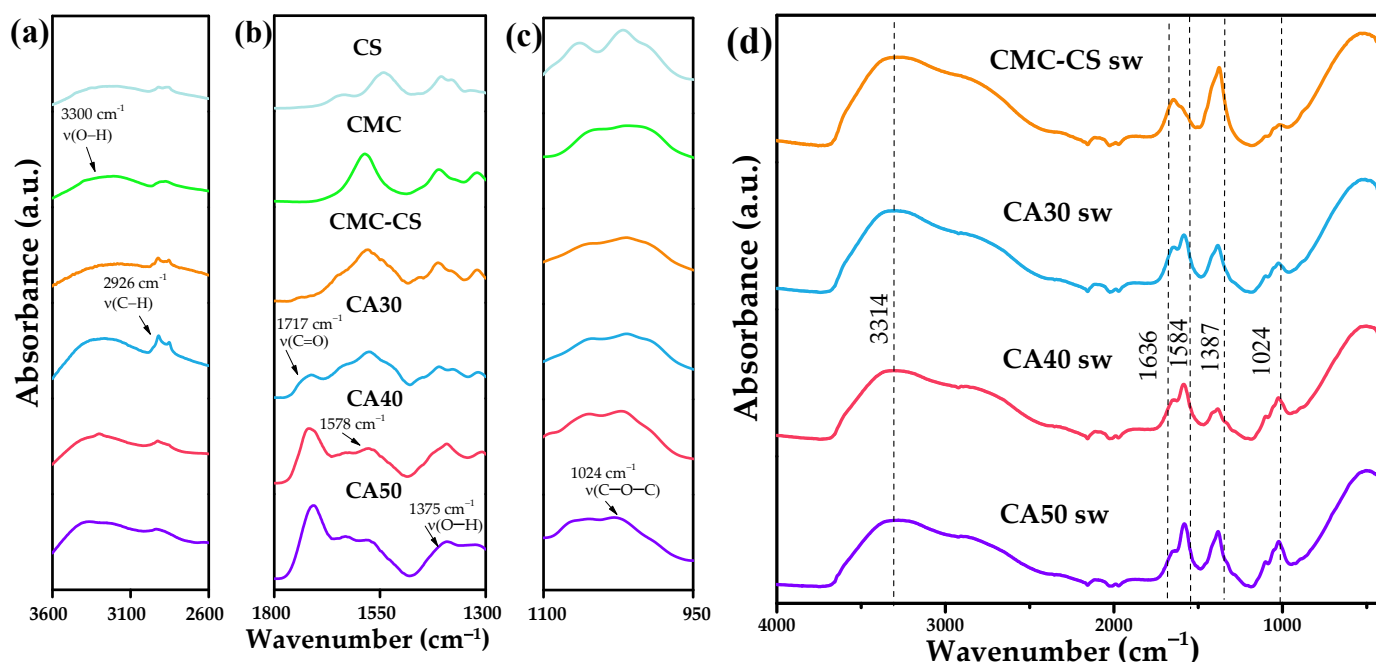
Figure 3. ATR-FTIR spectra of (**a**) CS, (**b**) CMC, (**c**) CMC–CS, and (**d**) CMC–CS sw hydrogels at different CA proportions.

As for the swollen hydrogels (Figure 3b), the first relevant observed change was in the –OH and –C–H region, with an increase in the broad band due to the insertion of water, pointing to a higher amount and stronger hydrogen bonds within the polymeric matrix [43]. The band at 1636 cm^{-1} mapped to the frequency of the water bending mode [61]. The characteristic C=O peak shifted to 1584 cm^{-1}, probably because of an amorphous state [62] due to the presence of hydroxyl groups of the KOH. Santos et al. [41] reported that the oxygen atoms of the KOH and the C=O groups of the polymer were strong electron donors due to the presence of available lone pairs of electrons, pointing to coordination of the K$^+$ cations, with these groups forming complexes such as C=O$\cdots$K$^+$ or C–O$\cdots$K$^+$. The fingerprint region indicated the skeletal signals of the glycosidic bonds, where the C–O–C vibration of the pyramidal ring at 1024 cm^{-1} was shown to be reduced in intensity, evidencing the change in the shape and intensity of the C–H and C–O–C peaks [63]. This reduction can be explained by the interaction between the Lewis OH– base and Lewis acid of the CA, with the smaller band for the membrane with less CA content, pointing to the preservation of the polysaccharide chains when more CA was added to the matrix.

3.3.2. XRD Analysis

The XRD pattern from pure CMC is reported to exhibit a diffraction peak at $2\theta = 19.59°$ [64], while for CS it presents characteristic peaks at 10.18° and 20.16°. These values indicate a semicrystalline nature for the polymers [65]. In our study, the peak at 10.18° disappeared from the diffractograms, and the most relevant peak obtained was at $2\theta = 21°$, exhibiting a broad shape (Figure 4). This peak points to the amorphous nature of the membranes when compared with the pure polymers [39,59]. Then, when analyzing the swollen membranes, the degree of crystallinity (X_c) decreased due to the addition of the KOH solution. The formed complex between the polysaccharide chains and the potassium cations could explain this behavior. Hence, the decrease in the crystallinity could be explained by the destruction of the hydrogen bonding in the matrix [66].
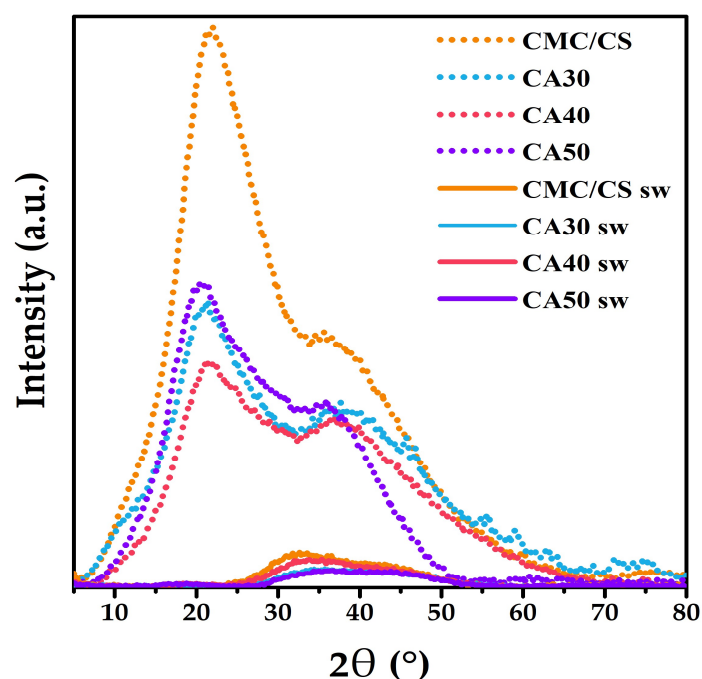
Figure 4. XRD patterns of the CMC-CS and CMC-CS sw hydrogels at different CA proportions.

The addition of the CA crosslinker increased the amorphousness of the hydrogels, obtaining 15.6% of the crystallinity in the case of the CA50 unswollen membrane (Table 2). Moreover, with the absorption of the KOH, it was observed that X_c decreased. The smallest degree of crystallinity was obtained for the CA40 sw hydrogel, reaching 4.6%, while the values for the CA30 sw and CA50 sw membranes were 5.2% and 4.7%, respectively. The degree of crystallinity is important, as it is related to the hydrogels' swelling behavior [67]. Additionally, the ionic conductivity suffered an improvement, as the crystallinity decreased since the ions have low mobility in the crystalline phases [68,69]. With the increased amorphousness, more voids were present, which is relevant to obtain higher ionic conductivity values [70].

**Table 2.** Crystallinity degree (X_c) calculated from the XRD patterns.

Membranes	X_c (%)
CMC–CS	17.9
CA30	15.5
CA40	14.4
CA50	15.6
CMC–CS sw	10.7
CA30 sw	5.2
CA40 sw	4.6
CA50 sw	4.7

3.3.3. SEM Micrographs and BET Analysis

For the uncrosslinked membrane CMC-CS, more smoothness and uniformity of the surface was shown, with few lumps presented on it (Figure 5a,b). This observation suggests good miscibility, homogeneity, and interaction of the polymers that form the membrane, leading to compaction of the microstructure [71]. For the crosslinked membrane CA50, a chapped surface with pleats, granules, and some orifices (macroporous) was observed. Wang et al. [72] reported similar surface structures related to the crosslinking degree achieved by polyethyleneimine/poly(vinyl alcohol) composites. Otherwise, Ritonga et al. [73] reported that the presence of uneven granules dispersed on the surface of hydrogels composed of chitosan-ethylenediaminetetraacetic acid, which has been iden-

tified as a crosslinker. The N_2 adsorption–desorption isotherms for the hydrogels were obtained (Figure S1). A mix of type II and type III isotherms was observed, with a low superficial area ranging from 3.3 m^2/g for the CMC-CS membrane to 2.0 m^2/g for the CA50 membrane. The herein obtained results suggest the obtention of nonporous or macroporous materials with a low relationship between the adsorbent and adsorbate. Hence, the swelling behavior when the membranes were hydrated with KOH solutions can be explained by a phenomenon of absorption rather than adsorption, indeed related to the crosslinking degree [39].
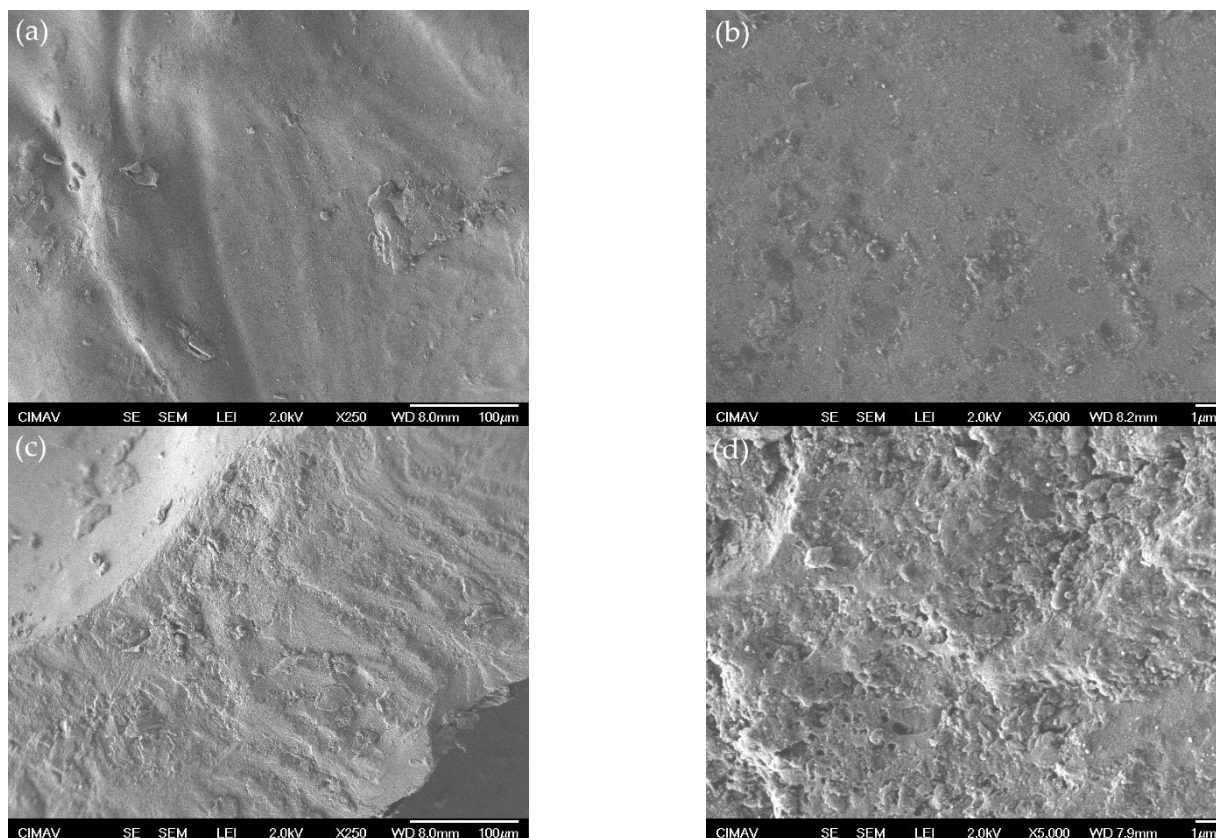
Figure 5. SEM micrographs of the CMC-CS membrane at (**a**) 250× and (**b**) 5000× and the CA50 membrane at (**c**) 250× and (**d**) 5000×.

3.4. Thermal Characterization

The CMC-CS membrane shows three degradation regions starting at 40, 130, and 330 °C (Figure 6). The first loss (17.8 wt.%) was attributed to the internal loss of water that the polymeric matrix undergoes. The second and third losses were linked to the degradation of the polymeric backbone. The second weight loss was also related to carbon formation [74,75]. Comparing our curves for the dry membranes with the curves obtained by Uyanga et al. [39] for pure polymers, it can be seen that the degradation regions coincide but in our case with an increase in the thermal stability. From ~450 °C onwards, a stable behavior was observed, with a remaining residue of ~34.6 wt.% for the CMC-CS membrane and 26.4 wt.% for the CA50 membrane, suggesting an increase in the carbon yield with the increasing CA content in the hydrogel. The carbon yield is influenced by the chemical bonds and functional groups in a sample [76].
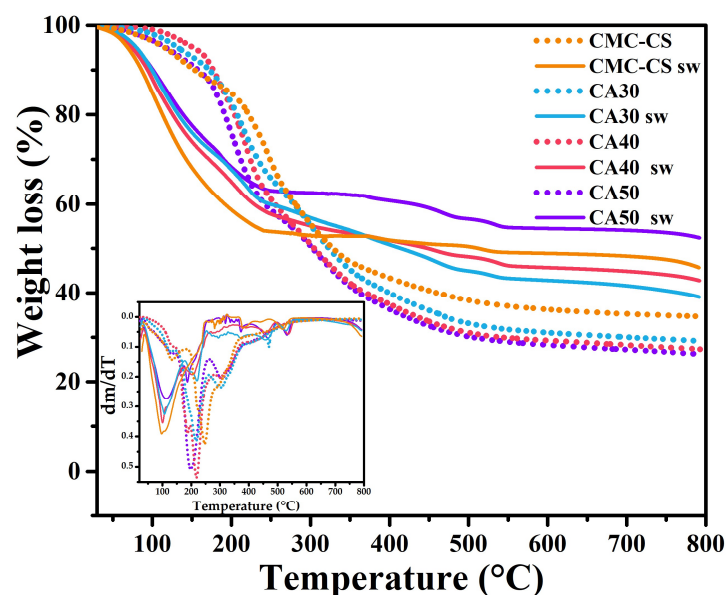
Figure 6. TGA curves of the CMC-CS and CMC-CS sw hydrogels at different CA proportions. Inset: DTGA curves of the electrolytes.

In the case of the swelled membranes in KOH solution, the loss of absorbed water by the hydrophilic groups in the polymer chains began at 47.7, 50.8, 53.6, and 56.6 °C for the CMC-CS sw, CA40 sw, CA50 sw, and CA30 sw, respectively. It was observed from the DTGA curves (Figure 6 inset) that the minimum peak shifted from 96.8 to 112.8 °C as more CA was added to the crosslinked membrane (CA50). That shift of the minimum peak is evidence of an increased thermal stability and higher water retention in the polymer matrix [62]. This can be explained by the higher degree of esterification (discussed in Section 3.1), since with the presence of more ester bonds in the polymer chain, a more reinforced structure is obtained, leading to stronger internal bonds that require more heat to undergo the regions of degradation. The next range of the matrix's degradation began at 240 °C. The weight loss was 45.9%, 41.5%, 39.64%, and 36.7% for CMC-CS sw, CA30 sw, CA40 sw, and CA50 sw, respectively. These losses originated from the degradation of the saccharide structure of the molecule [77]. The last region found from 516 to 537 °C shows the modification of the chemical structure produced by the oxygen-containing KOH molecule. The intensity of this peak was related to the KOH swelling behavior of the membranes. The higher residue percentage in the swelled hydrogels in comparison to the dried membranes could suggest the presence of potassium salts formed when KOH is decomposed [78].

The intermolecular interaction of the components could be evidenced in the DSC curves of the dried hydrogels (Figure S2a). For the CMC-CS hydrogel, it was evidenced an endothermic peak at 110 °C, attributable to heat absorption by water evaporation from the hydrogels [40]. Moreover, another endothermic peak was depicted at 204 °C, referable to the thermal degradation of the polymers [79]. However, for the CMC-CS-CA hydrogels, this peak shifted to lower values (194 °C), further confirming crosslinking. Beyond 235 °C, the last peak turned into an exothermic peak for all hydrogels. This phenomenon has been reported to be associated with CS structure debonding and the decomposition of its amine unit [80]. In terms of the soaked hydrogels, the increase in the intensity of the DSC curves (Figure S2b) points to firmer internal bonds related to the addition of CA, requiring more heat to evaporate the moisture and break the membrane bonds and, finally, leading to the thermal degradation of the structures [39].

3.5. Electrochemical Characterization

3.5.1. Influence of the CA Content on the Ionic Conductivity

The ionic conductivity (σ) was studied as a function of the temperature for all of the swollen hydrogels (Figure 7). For Arrhenius to be suitable, the plots of $\ln(\sigma)$ versus $1000/T$ should follow a linear fitting in the chosen temperature range. This linearity points to a thermally assisted conduction [81]. In this type of conduction, the energy barrier E_a needs to be surmounted for the ion to move from one site to another [82]. The highest value of E_a was obtained for the CMC-CS sw hydrogel, with 0.21 eV. Smaller values of 0.14 and 0.18 eV were obtained for the crosslinked hydrogels CA40 sw and CA30 sw, respectively (Table 3). Moreover, the Arrhenius behavior in the CMC-CS sw hydrogel was lost at 50 °C, whereas for the CMC-CS-CA sw membranes, they achieved linearity until 60 °C, suggesting an enhanced stability of the conduction process for the synthesized hydrogels.
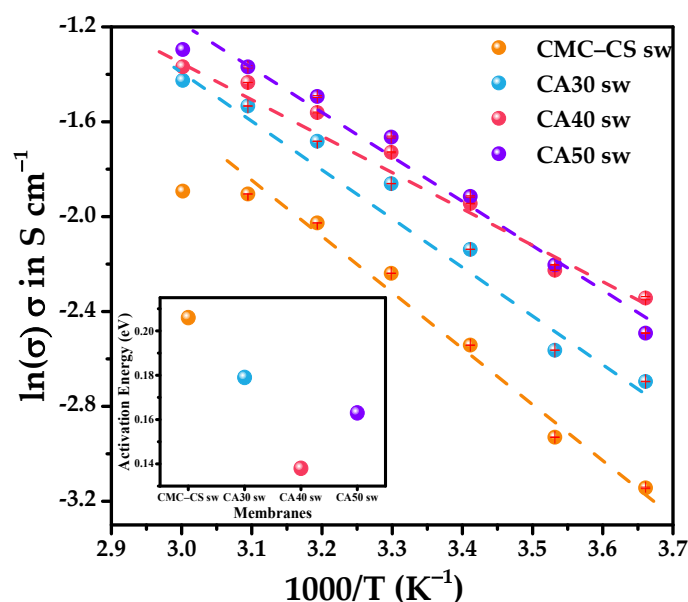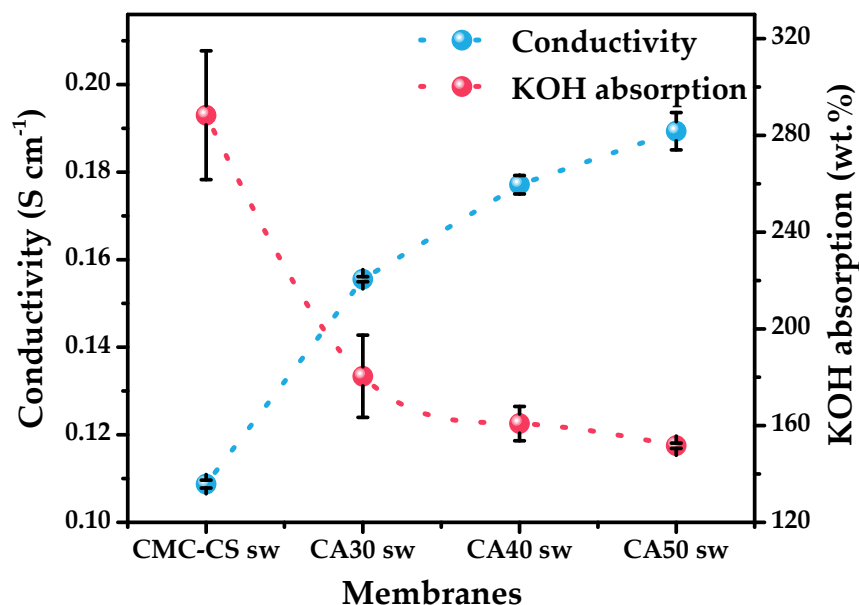

Figure 7. Ionic conductivity of the CMC-CS sw electrolytes at different temperatures. Inset: Activation energy (E_a) of the CMC-CS sw electrolytes.

Table 3. Swelling ratio and some electrochemical values obtained for the CMC-CS and CMC-CS-CA sw electrolytes. Ionic conductivity values were obtained at T = 30 °C.

Electrolyte	KOH Absorption (%)	E_a (eV)	σ (S·cm^{-1})
CMC-CS sw	288.35 ± 26.64	0.21	0.11
CA30 sw	180.40 ± 17.01	0.18	0.16
CA40 sw	160.83 ± 7.10	0.14	0.18
CA50 sw	151.69 ± 1.09	0.16	0.19

The results show the swelled KOH to be inversely proportional to the increase in ionic conductivity, obtaining a maximum of 189 mS cm^{-1} for the CA50 sw hydrogel (Figure 8). This apparent contradictory behavior can be explained by the capability of the membrane to retain the swelled KOH when it is pressed between the electrodes and its further integrity. These values follow the trend of the decrease in the crystallinity caused by the KOH solution, which was already discussed in Section 3.3.2. This effect was enhanced when the temperature increased, generating a more structural relaxation of the polymer chains and expanding the free volume, causing an increase in the conductivity as evidenced in Figure 7, obtaining a conductivity of 273 mS cm^{-1} for the CA50 sw hydrogel at 60 °C. Therefore, the results agree with reports of the decrease in the crystallinity to be inversely proportional

with the increase in the ionic conductivity [83,84]. The obtained values for σ show a substantial increase from previous studies in the field, where ionic conductivities of less than 10^{-3} S·cm^{-1} were reported [85–89], pointing to the applicability of these membranes in electrochemical applications. Achieving a high ionic conductivity allows for more ions to pass through at a given time, improving the capacity at higher discharge rates [90], which is also important for obtaining a high energy density [91].

Figure 8. Comparison between the ionic conductive values and KOH absorption behavior of the CMC-CS sw hydrogels at different CA proportions.
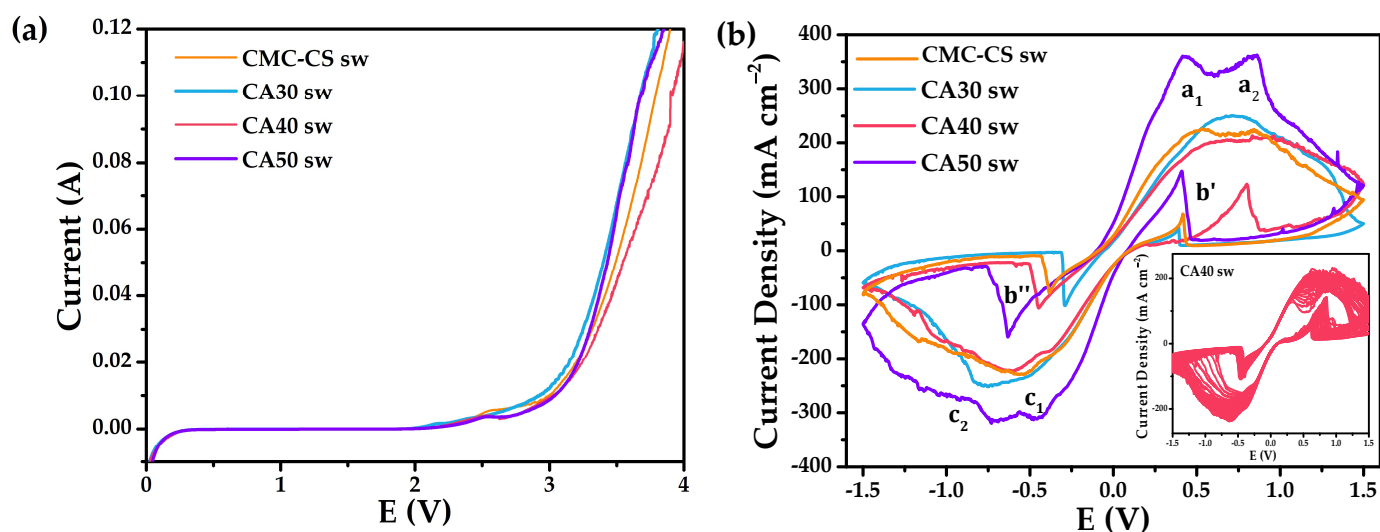
3.5.2. Linear Sweep and Cyclic Voltammetry (CV)

It can be evidenced from the linear sweep voltammetry (LSV) studies how the electrolytes were stable in a long electrochemical potential window (Figure 9a), with the best window obtained for the CA50 membrane, which reached up to approximately +2.1 V, while the other electrolytes resulted in being also highly stable in comparison with a liquid electrolyte, for which the electrochemical window (1.23 V) is restricted due to the water electrolysis. The cyclic voltammetry (CV) studies were performed in an electrochemical stability window in the range of −1.5 to 1.5 V to study Zn^{2+} conduction and reversible equilibrium between the zinc metal and the zinc ions present inside the CMC-CS sw hydrogels, as presented in Figure 9b. When analyzing the peaks' shape, a quasi-reversible behavior for the redox processes was evidenced; the cathodic peak corresponded to the reduction process of Zn^{2+} to Zn^0, while the anodic peak was attributed to zinc oxidation to Zn^{2+} cations [43]. The oxidation/reduction reactions were evidenced for all of the membranes according to the peaks in the CV plot as evidence of the establishment of the reversibility of the Zn/Zn^{2+} couple. Two peaks split into both anodic (a_1 and a_2) and cathodic (c_1 and c_2) branches were observed. The first peak in the anodic branch (a_1) was highly reported for alkaline electrolytes [90], being as follows:

$$Zn + 4\,OH^- \rightleftharpoons Zn(OH)_4{}^{2-} + 2\,e^-$$

Whereas for the second peak, a_2, Cai et al. [92] associated it to the formation of $Zn(OH)_3{}^-$ complexes due to the depletion of OH^- anions near the electrode surface, creating a prepassive layer at a more positive potential than a_1. For the cathode peaks, the reverse reactions were happening. The inverse peak b′ in the cathodic branch was reported to occur due to the oxidation of Zn after some dissolution of the passive film deposited

on the surface of the Zn electrode that was released during the cathodic sweep. The same occurred for peak b″ in the anodic sweep [41].


Figure 9. (**a**) Linear sweep voltammetry studies for the CMC–CS sw hydrogels at different CA proportions; (**b**) cyclic voltammograms of the swollen hydrogels at ambient temperature. Inset: 40 consecutive cycles of the CA40 sw membrane.

A maximum peak of intensity at 225 mA·cm^{-2} for the CMC-CS sw hydrogel was obtained, while for the CA50 sw membrane it achieved 360 mA·cm^{-2}. The large separation in peak potentials is reported to be due to the absence of reference electrode used, typical for the evaluation of gel PEs [93,94]. For all the membranes, stability is evidenced when performing 40 consecutive cycles, pointing to a good electrochemical behavior and the reversibility of the system. The presented results indicate an improvement of the fast-ionic motion across the electrolyte matrix, since the intensity values are reported to depend on the number of electrons transferred between the redox species and the electrode, which depends on the ions' movement [43,95]. The ionic conductive behavior of these type of PEs has been reported to be due to the heteroatoms from CMC and CS donating electron pairs from s orbitals to Lewis's acids, forming a complex–transport system [41]. Thus, it points to the applicability of the hydrogels in electrochemical devices.

3.6. Zn/Hydrogel/Air Battery

The primary ZAB was constructed using a previously reported configuration [96], without the use of the reservoir, being replaced by the hydrogel electrolytes proposed in this work (Figure 10e). The open circuit potential for all of the membranes reached values of 1.46 V. The discharge and power densities displayed in Figure 10a showed clear differences between the use of the CMC-CS sw membrane and the crosslinked membranes, with double the power density for the CA50 sw membrane (85 mW cm^{-2}) compared to the noncrosslinked membrane (40 mW cm^{-2}). These results show an enhancement in the power density of the system when compared with the use of KOH 6 M as an electrolyte, where a power density of 28 mW cm^{-2} was reported by Díaz-Patiño et al. [97]. The CMC-CS sw hydrogel required the greatest electrical work at the demanding current densities in the stability tests at different current densities (Figure 10b), reflected in the higher overpotentials. In comparison, the CA50 sw membrane required lower overpotentials to provide the fixed current densities. In addition, the ZAB using the CMC-CS sw electrolyte was unable to sustain operation at current densities of 10 mA·cm^{-2}. Table 4 shows the battery performance obtained in this work compared to other reports that used polymers in their electrolyte system.
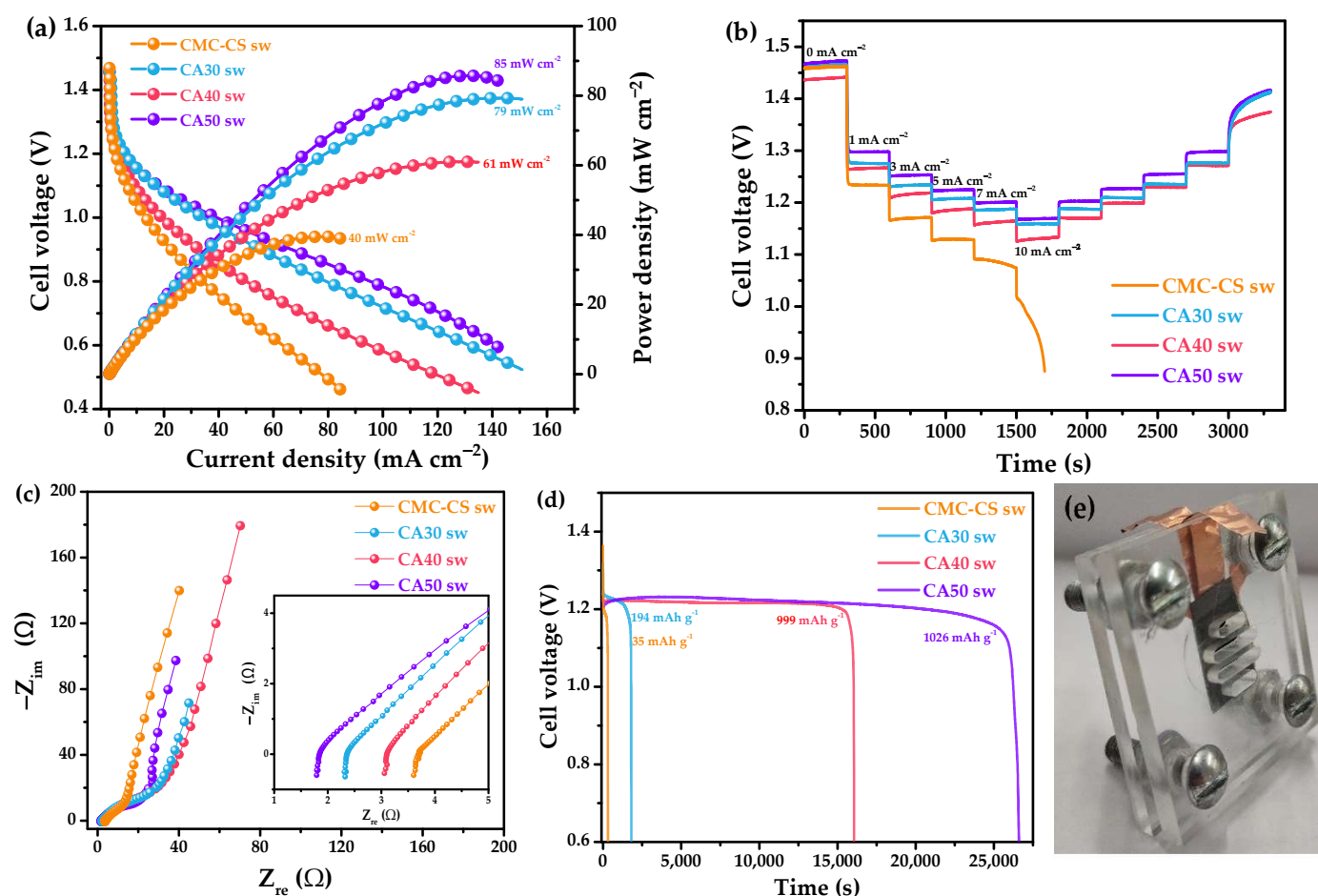
Figure 10. (**a**) Discharge and power density curves for the battery operated with the Zn foil as an anode and Pt/C as a cathode and the synthetized hydrogels; (**b**) discharge tests at selected current densities; (**c**) potential electrochemical impedance spectroscopy studies; (**d**) discharge performance at 3 mA cm^{-2}; (**e**) photograph of the assembled device.

Table 4. Battery performance of some Zinc–air batteries with polymer electrolytes.

Electrolyte	Ionic Conductivity (S cm^{-1})	Bulk Resistance (Ω)	Specific Capacitance (mA·h g^{-1})	Power Density (mW cm^{-2})	Reference
Chitosan-PDDA-GA KOH	0.02	~1.00	-	48.9	[98]
QA-functionalized nanocellulose-GO-KOH	0.04	-	-	44.1	[99]
PVA-PEG-SiO$_2$ KOH	0.06	~1.30	720.6	62.6	[100]
PVA-NH$_4$Cl-ZnCl	0.07	2.16	-	~8	[101]
CS-PVA KOH	0.11	1.06	221.6	-	[102]
CMC-CS-CA KOH	0.19	1.85	1026	85	This work

In terms of the bulk resistances (R$_b$) of the ZABs (Figure 10c), values of 3.65 Ω for the CMC-CS sw membrane and 1.85 Ω for the CA50 sw membrane were obtained. This decreasing pattern of R$_b$ was due to the increasing of the charge carriers and the OH$^-$ ions with an increased SR [103]. The discharge time of the battery using the CA50 sw reached a 7.4 h set time for the discharge process (Figure 10d), while for the CMC-CS sw membrane, it only took 4 min to finish discharging. The average nominal voltages at the flat plateau region ranged from 1.23 V for the CA50 sw hydrogel to 1.20 V for the CMC-CS sw hydrogel before hitting cutoff voltages of 1.19 and 1.18 V, respectively. The voltage values decreased

slightly in the plateau region, possibly due to the concentration polarization caused by salt depletion or accumulation within the cell [104]. The maximum specific capacitance obtained was 1026 mA·h g^{-1} for the battery assembled with the CA50 sw electrolyte.

4. Conclusions

The esterification/crosslinking reaction for the CMC-CS-CA hydrogels was achieved through the synthesis proposed in this work, confirmed by ATR-FTIR. The swelling behavior of the noncrosslinked hydrogel had a higher swelling ratio than its counterparts with citric acid. However, this higher capacity came along with low structural integrity when used in battery assemblies. With the addition of CA, a superior structural stability of the membranes was obtained. The structural characterization carried out suggested a higher thermal stability and a decrease in the degree of crystallinity of the crosslinked membranes. The absorption and nonadsorption mechanism was confirmed through the study of N_2 adsorption/desorption processes.

The values of the ionic conductivity and current improved with the proposed hydrogels compared to the noncrosslinked electrolyte, confirmed by the electrochemical characterization by electrochemical impedance spectroscopy and cyclic voltammetry. Arrhenius behavior was confirmed in the range of 0 to 60 °C for the crosslinked membranes, and a maximum value of 0.19 S·cm^{-1} was found at 30 °C. In addition, the cyclic voltammetry studies confirmed a quasi-reversible behavior, with maximum intensity peaks of 360 mA cm^{-2}, as evidence of the high ionic transfer achieved by the CA50 sw hydrogel. The synthesized hydrogels were finally tested in a zinc–air battery, with high performance in terms of power densities, bulk resistances, and discharge times. The obtained results show that these hydrogels are suitable candidates for use in energy storage devices.

References

1. Liu, F.; Chen, Z.; Fang, G.; Wang, Z.; Cai, Y.; Tang, B.; Zhou, J.; Liang, S. V2O5 Nanospheres with Mixed Vanadium Valences as High Electrochemically Active Aqueous Zinc-Ion Battery Cathode. *Nano-Micro Lett.* **2019**, *11*, 1–11. [CrossRef]
2. Deivanayagam, R.; Ingram, B.J.; Shahbazian-Yassar, R. Progress in development of electrolytes for magnesium batteries. *Energy Storage Mater.* **2019**, *21*, 136–153. [CrossRef]

3. Wang, F.; Borodin, O.; Gao, T.; Fan, X.; Sun, W.; Han, F.; Faraone, A.; Dura, J.A.; Xu, K.; Wang, C. Highly reversible zinc metal anode for aqueous batteries. *Nat. Mater.* **2018**, *17*, 543–549. [CrossRef] [PubMed]

4. Boaretto, N.; Meabe, L.; Martinez-Ibañez, M.; Armand, M.; Zhang, H. Review—Polymer Electrolytes for Rechargeable Batteries: From Nanocomposite to Nanohybrid. *J. Electrochem. Soc.* **2020**, *167*, 070524. [CrossRef]

5. Fang, G.; Zhu, C.; Chen, M.; Zhou, J.; Tang, B.; Cao, X.; Zheng, X.; Pan, A.; Liang, S. Suppressing Manganese Dissolution in Potassium Manganate with Rich Oxygen Defects Engaged High-Energy-Density and Durable Aqueous Zinc-Ion Battery. *Adv. Funct. Mater.* **2019**, *29*, 1808375. [CrossRef]

6. Kundu, D.; Adams, B.D.; Duffort, V.; Vajargah, S.H.; Nazar, L.F. A high-capacity and long-life aqueous rechargeable zinc battery using a metal oxide intercalation cathode. *Nat. Energy* **2016**, *1*, 16119. [CrossRef]

7. Pan, H.; Shao, Y.; Yan, P.; Cheng, Y.; Han, K.S.; Nie, Z.; Wang, C.; Yang, J.; Li, X.; Bhattacharya, P.; et al. Reversible aqueous zinc/manganese oxide energy storage from conversion reactions. *Nat. Energy* **2016**, *1*, 16039. [CrossRef]

8. Zhang, Y.; Liu, Y.; Liu, Z.; Wu, X.; Wen, Y.; Chen, H.; Ni, X.; Liu, G.; Huang, J.; Peng, S. MnO2 cathode materials with the improved stability via nitrogen doping for aqueous zinc-ion batteries. *J. Energy Chem.* **2022**, *64*, 23–32. [CrossRef]

9. Li, Y.; Dai, H. Recent advances in zinc–air batteries. *Chem. Soc. Rev.* **2014**, *43*, 5257–5275. [CrossRef] [PubMed]

10. Li, S.; Guo, H.; He, S.; Yang, H.; Liu, K.; Duan, G.; Jiang, S. Advanced electrospun nanofibers as bifunctional electrocatalysts for flexible metal-air (O$_2$) batteries: Opportunities and challenges. *Mater. Des.* **2022**, *214*, 110406. [CrossRef]

11. Li, D.; Lv, Q.; Zhang, C.; Zhou, W.; Guo, H.; Jiang, S.; Li, Z. The Effect of Electrode Thickness on the High-Current Discharge and Long-Term Cycle Performance of a Lithium-Ion Battery. *Batteries* **2022**, *8*, 101. [CrossRef]

12. Zaghib, K.; Song, S.-W.; Singh, K.; Yao, Y.; Ichikawa, T.; Jain, A.; Singh, R. Zinc as a Promising Anodic Material for All-Solid-State Lithium-Ion Batteries. *Batteries* **2022**, *8*, 113. [CrossRef]

13. Lu, C.-T.; Zhu, Z.-Y.; Chen, S.-W.; Chang, Y.-L.; Hsueh, K.-L. Effects of Cell Design Parameters on Zinc-Air Battery Performance. *Batteries* **2022**, *8*, 92. [CrossRef]

14. Parveen, N.; Ansari, S.A.; Ansari, M.Z.; Ansari, M.O. Manganese oxide as an effective electrode material for energy storage: A review. *Environ. Chem. Lett.* **2021**, *20*, 283–309. [CrossRef]

15. He, W.; Zuo, S.; Xu, X.; Zeng, L.; Liu, L.; Zhao, W.; Liu, J. Challenges and strategies of zinc anode for aqueous zinc-ion batteries. *Mater. Chem. Front.* **2021**, *5*, 2201–2217. [CrossRef]

16. Ye, T.; Li, L.; Zhang, Y. Recent Progress in Solid Electrolytes for Energy Storage Devices. *Adv. Funct. Mater.* **2020**, *30*, 2000077. [CrossRef]

17. Zhao, C.; Liu, L.; Qi, X.; Lu, Y.; Wu, F.; Zhao, J.; Yu, Y.; Hu, Y.-S.; Chen, L. Solid-State Sodium Batteries. *Adv. Energy Mater.* **2018**, *8*, 1703012. [CrossRef]

18. Xu, Z.; Wu, M. Toward Dendrite-Free Deposition in Zinc-Based Flow Batteries: Status and Prospects. *Batteries* **2022**, *8*, 117. [CrossRef]

19. Wood, K.N.; Kazyak, E.; Chadwick, A.F.; Chen, K.-H.; Zhang, J.-G.; Thornton, K.; Dasgupta, N.P. Dendrites and Pits: Untangling the Complex Behavior of Lithium Metal Anodes through Operando Video Microscopy. *ACS Cent. Sci.* **2016**, *2*, 790–801. [CrossRef]

20. Wu, F.; Yuan, Y.-X.; Cheng, X.-B.; Bai, Y.; Li, Y.; Wu, C.; Zhang, Q. Perspectives for restraining harsh lithium dendrite growth: Towards robust lithium metal anodes. *Energy Storage Mater.* **2018**, *15*, 148–170. [CrossRef]

21. Zhang, H.; Li, C.; Piszcz, M.; Coya, E.; Rojo, T.; Rodriguez-Martinez, L.M.; Armand, M.; Zhou, Z. Single lithium-ion conducting solid polymer electrolytes: Advances and perspectives. *Chem. Soc. Rev.* **2017**, *46*, 797–815. [CrossRef] [PubMed]

22. Hallinan, D.T.; Villaluenga, I.; Balsara, N.P. Polymer and composite electrolytes. *MRS Bull.* **2018**, *43*, 775–781. [CrossRef]

23. Mindemark, J.; Lacey, M.J.; Bowden, T.; Brandell, D. Beyond PEO—Alternative host materials for Li + -conducting solid polymer electrolytes. *Prog. Polym. Sci.* **2018**, *81*, 114–143. [CrossRef]

24. Bósquez-Cáceres, M.F.; Hidalgo-Bonilla, S.; Córdova, V.M.; Michell, R.M.; Tafur, J.P. Nanocomposite Polymer Electrolytes for Zinc and Magnesium Batteries: From Synthetic to Biopolymers. *Polymers* **2021**, *13*, 4284. [CrossRef]

25. Mo, F.; Guo, B.; Ling, W.; Wei, J.; Chen, L.; Yu, S.; Liang, G. Recent Progress and Challenges of Flexible Zn-Based Batteries with Polymer Electrolyte. *Batteries* **2022**, *8*, 59. [CrossRef]

26. Wu, K.; Huang, J.; Yi, J.; Liu, X.; Liu, Y.; Wang, Y.; Zhang, J.; Xia, Y. Recent Advances in Polymer Electrolytes for Zinc Ion Batteries: Mechanisms, Properties, and Perspectives. *Adv. Energy Mater.* **2020**, *10*, 209–216. [CrossRef]

27. Lorca, S.; Santos, F.; Fernández Romero, A.J. A Review of the Use of GPEs in Zinc-Based Batteries. A Step Closer to Wearable Electronic Gadgets and Smart Textiles. *Polymers* **2020**, *12*, 2812. [CrossRef]

28. Mohamed, N.S.; Subban, R.H.Y.; Arof, A.K. Polymer batteries fabricated from lithium complexed acetylated chitosan. *J. Power Sources* **1995**, *56*, 153–156. [CrossRef]

29. Saad, E.M.; Elshaarawy, R.F.; Mahmoud, S.A.; El-Moselhy, K.M. New Ulva lactuca Algae Based Chitosan Bio-composites for Bioremediation of Cd(II) Ions. *J. Bioresour. Bioprod.* **2021**, *6*, 223–242. [CrossRef]

30. Madni, A.; Kousar, R.; Naeem, N.; Wahid, F. Recent advancements in applications of chitosan-based biomaterials for skin tissue engineering. *J. Bioresour. Bioprod.* **2021**, *6*, 11–25. [CrossRef]

31. Rosca, C.; Popa, M.I.; Lisa, G.; Chitanu, G.C. Interaction of chitosan with natural or synthetic anionic polyelectrolytes. 1. The chitosan–carboxymethylcellulose complex. *Carbohydr. Polym.* **2005**, *62*, 35–41. [CrossRef]

32. Shang, J.; Shao, Z.; Chen, X. Electrical Behavior of a Natural Polyelectrolyte Hydrogel: Chitosan/Carboxymethylcellulose Hydrogel. *Biomacromolecules* **2008**, *9*, 1208–1213. [CrossRef] [PubMed]

33. Bakar, N.Y.; Isa, M.I.N. Potential of Ionic Conductivity and Transport Properties Solid Biopolymer Electrolytes Based Carboxy Methylcellulose/Chitosan Polymer Blend Doped with Dodecyltrimethyl Ammonium Bromide. *Res. J. Recent Sci.* **2014**, *3*, 74.

34. Rani, M.S.A.; Mohamed, N.S.; Isa, M.I.N. Investigation of the Ionic Conduction Mechanism in Carboxymethyl Cellulose/Chitosan Biopolymer Blend Electrolyte Impregnated with Ammonium Nitrate. *Int. J. Polym. Anal. Charact.* **2015**, *20*, 491–503. [CrossRef]

35. Wang, Z.; Li, H.; Tang, Z.; Liu, Z.; Ruan, Z.; Ma, L.; Yang, Q.; Wang, D.; Zhi, C.; Wang, Z.F.; et al. Hydrogel Electrolytes for Flexible Aqueous Energy Storage Devices. *Adv. Funct. Mater.* **2018**, *28*, 1804560. [CrossRef]

36. Liu, J.; Ahmed, S.; Khanam, Z.; Wang, T.; Song, S. Ionic Liquid-Incorporated Zn-Ion Conducting Polymer Electrolyte Membranes. *Polymers* **2020**, *12*, 1755. [CrossRef]

37. Manzoor, K.; Ahmad, M.; Ahmad, S.; Ikram, S. Removal of Pb(ii) and Cd(ii) from wastewater using arginine cross-linked chitosan–carboxymethyl cellulose beads as green adsorbent. *RSC Adv.* **2019**, *9*, 7890–7902. [CrossRef]

38. Salama, H.E.; Abdel Aziz, M.S.; Alsehli, M. Carboxymethyl cellulose/sodium alginate/chitosan biguanidine hydrochloride ternary system for edible coatings. *Int. J. Biol. Macromol.* **2019**, *139*, 614–620. [CrossRef]

39. Uyanga, K.A.; Daoud, W.A. Green and sustainable carboxymethyl cellulose-chitosan composite hydrogels: Effect of crosslinker on microstructure. *Cellulose* **2021**, *28*, 5493–5512. [CrossRef]

40. Uyanga, K.A.; Daoud, W.A. Carboxymethyl cellulose-chitosan composite hydrogel: Modelling and experimental study of the effect of composition on microstructure and swelling response. *Int. J. Biol. Macromol.* **2021**, *181*, 1010–1022. [CrossRef]

41. Santos, F.; Tafur, J.P.; Abad, J.; Fernández Romero, A.J. Structural modifications and ionic transport of PVA-KOH hydrogels applied in Zn/Air batteries. *J. Electroanal. Chem.* **2019**, *850*, 113380. [CrossRef]

42. Lewandowski, A.; Skorupska, K.; Malinska, J. Novel poly(vinyl alcohol)–KOH–H2O alkaline polymer electrolyte. *Solid State Ion.* **2000**, *133*, 265–271. [CrossRef]

43. Velez, A.A.I.; Reyes, E.; Diaz-Barrios, A.; Santos, F.; Fernández Romero, A.J.; Tafur, J.P. Properties of the PVA-VAVTD KOH Blend as a Gel Polymer Electrolyte for Zinc Batteries. *Gels* **2021**, *7*, 256. [CrossRef]

44. Calderón Salas, L.A.; De Lima Eljuri, L.; Caetano Sousa, M. *Synthesis and Characterization of Chemically Crosslinked Carboxymethyl Cellulose/Chitosan Composite Hydrogels*; Universidad de Investigación de Tecnología Experimental Yachay: Urcuqui, Ecuador, 2021.

45. Putz, H.; Brandenburg, K. Match!—Phase Analysis Using Powder Diffraction. Available online: https://www.crystalimpact.de/match (accessed on 16 August 2022).

46. Nuernberg, R.B. Numerical comparison of usual Arrhenius-type equations for modeling ionic transport in solids. *Ionics* **2020**, *26*, 2405–2412. [CrossRef]

47. Chandra Roy, J.; Ferri, A.; Giraud, S.; Jinping, G.; Salaün, F. Chitosan–Carboxymethylcellulose-Based Polyelectrolyte Complexation and Microcapsule Shell Formulation. *Int. J. Mol. Sci.* **2018**, *19*, 2521. [CrossRef]

48. Seki, Y.; Altinisik, A.; Demircioğlu, B.; Tetik, C. Carboxymethylcellulose (CMC)–hydroxyethylcellulose (HEC) based hydrogels: Synthesis and characterization. *Cellulose* **2014**, *21*, 1689–1698. [CrossRef]

49. Fekete, T.; Borsa, J.; Takács, E.; Wojnárovits, L. Synthesis of carboxymethylcellulose/acrylic acid hydrogels with superabsorbent properties by radiation-initiated crosslinking. *Radiat. Phys. Chem.* **2016**, *124*, 135–139. [CrossRef]

50. Bajpai, J.; Mishra, S.; Bajpai, A.K. Dynamics of controlled release of potassium nitrate from a highly swelling binary polymeric blend of alginate and carboxymethyl cellulose. *J. Appl. Polym. Sci.* **2007**, *106*, 961–972. [CrossRef]

51. Johns, J.; Rao, V. Mechanical Properties and Swelling Behavior of Cross-Linked Natural Rubber/Chitosan Blends. *Int. J. Polym. Anal. Charact.* **2009**, *14*, 508–526. [CrossRef]

52. Zhang, P.; Wang, K.; Pei, P.; Zuo, Y.; Wei, M.; Liu, X.; Xiao, Y.; Xiong, J. Selection of hydrogel electrolytes for flexible zinc–air batteries. *Mater. Today Chem.* **2021**, *21*, 100538. [CrossRef]

53. Pavia, D.L.; Lampman, G.M.; Kriz, G.S.; Vyvyan, J.R. *Introduction to Spectroscopy*, 5th ed.; Cengage Learning: Boston, MA, USA, 2013.

54. Kadir, M.F.Z.; Aspanut, Z.; Majid, S.R.; Arof, A.K. FTIR studies of plasticized poly(vinyl alcohol)–chitosan blend doped with NH4NO3 polymer electrolyte membrane. *Spectrochim. Acta Part A Mol. Biomol. Spectrosc.* **2011**, *78*, 1068–1074. [CrossRef] [PubMed]

55. Corazzari, I.; Nisticò, R.; Turci, F.; Faga, M.G.; Franzoso, F.; Tabasso, S.; Magnacca, G. Advanced physico-chemical characterization of chitosan by means of TGA coupled on-line with FTIR and GCMS: Thermal degradation and water adsorption capacity. *Polym. Degrad. Stab.* **2015**, *112*, 1–9. [CrossRef]

56. He, X.; Xu, H.; Li, H. Cr(VI) Removal from Aqueous Solution by Chitosan/Carboxylmethyl Cellulose/Silica Hybrid Membrane. *World J. Eng. Technol.* **2015**, *3*, 234–240. [CrossRef]

57. Biswal, D.R.; Singh, R.P. Characterisation of carboxymethyl cellulose and polyacrylamide graft copolymer. *Carbohydr. Polym.* **2004**, *57*, 379–387. [CrossRef]

58. Samsudin, A.S.; Kuan, E.C.H.; Isa, M.I.N. Investigation of the Potential of Proton-Conducting Biopolymer Electrolytes Based Methyl Cellulose-Glycolic Acid. *Int. J. Polym. Anal. Charact.* **2011**, *16*, 477–485. [CrossRef]

59. Rani, M.S.A.; Mohamed, N.S.; Isa, M.I.N. Characterization of Proton Conducting Carboxymethyl Cellulose/Chitosan Dual-Blend Based Biopolymer Electrolytes. *Mater. Sci. Forum* **2016**, *846*, 539–544. [CrossRef]

60. Harish Prashanth, K.V.; Kittur, F.S.; Tharanathan, R.N. Solid state structure of chitosan prepared under different N-deacetylating conditions. *Carbohydr. Polym.* **2002**, *50*, 27–33. [CrossRef]

61. Seki, T.; Chiang, K.-Y.; Yu, C.-C.; Yu, X.; Okuno, M.; Hunger, J.; Nagata, Y.; Bonn, M. The Bending Mode of Water: A Powerful Probe for Hydrogen Bond Structure of Aqueous Systems. *J. Phys. Chem. Lett.* **2020**, *11*, 8459–8469. [CrossRef]

62. Farinha, I.; Freitas, F. Chemically modified chitin, chitosan, and chitinous polymers as biomaterials. *Handb. Chitin Chitosan* **2020**, 43–69. [CrossRef]

63. Yu, M.; Li, J.; Wang, L. KOH-activated carbon aerogels derived from sodium carboxymethyl cellulose for high-performance supercapacitors and dye adsorption. *Chem. Eng. J.* **2017**, *310*, 300–306. [CrossRef]

64. Son, Y.-R.; Rhee, K.Y.; Park, S.-J. Influence of reduced graphene oxide on mechanical behaviors of sodium carboxymethyl cellulose. *Compos. Part B Eng.* **2015**, *83*, 36–42. [CrossRef]

65. Wang, Z.; Zheng, L.; Li, C.; Zhang, D.; Xiao, Y.; Guan, G.; Zhu, W. Modification of chitosan with monomethyl fumaric acid in an ionic liquid solution. *Carbohydr. Polym.* **2015**, *117*, 973–979. [CrossRef] [PubMed]

66. Aziz, S.B.; Abidin, Z.H.Z. Ion-transport study in nanocomposite solid polymer electrolytes based on chitosan: Electrical and dielectric analysis. *J. Appl. Polym. Sci.* **2015**, *132*, 41774. [CrossRef]

67. Zhang, J.; Wang, Y.; Zhang, L.; Zhang, R.; Liu, G.; Cheng, G. Understanding changes in cellulose crystalline structure of lignocellulosic biomass during ionic liquid pretreatment by XRD. *Bioresour. Technol.* **2014**, *151*, 402–405. [CrossRef]

68. Abdullah, O.G.H.; Hanna, R.R.; Salman, Y.A.K. Structural and electrical conductivity of CH:MC bio-poly-blend films: Optimize the perfect composition of the blend system. *Bull. Mater. Sci.* **2019**, *42*, 64. [CrossRef]

69. Saeed, M.A.M.; Gh Abdullah, O. Membranes. Effect of High Ammonium Salt Concentration and Temperature on the Structure, Morphology, and Ionic Conductivity of Proton-Conductor Solid Polymer Electrolytes Based PVA. *Membranes* **2020**, *10*, 262. [CrossRef]

70. Sing Ngai, K.; Ramesh, S.; Ramesh, K.; Ching Juan, J. A review of polymer electrolytes: Fundamental, approaches and applications. *Ionics* **2016**, *22*, 1259–1279. [CrossRef]

71. Grover, C.N.; Gwynne, J.H.; Pugh, N.; Hamaia, S.; Farndale, R.W.; Best, S.M.; Cameron, R.E. Crosslinking and composition influence the surface properties, mechanical stiffness and cell reactivity of collagen-based films. *Acta Biomater.* **2012**, *8*, 3080–3090. [CrossRef]

72. Wang, L.; Yang, X.; Daoud, W.A. High power-output mechanical energy harvester based on flexible and transparent Au nanoparticle-embedded polymer matrix. *Nano Energy* **2019**, *55*, 433–440. [CrossRef]

73. Ritonga, H.; Nurfadillah, A.; Rembon, F.S.; Ramadhan, L.O.A.N.; Nurdin, M. Preparation of Chitosan-EDTA hydrogel as soil conditioner for soybean plant (Glycine max). *Groundw. Sustain. Dev.* **2019**, *9*, 100277. [CrossRef]

74. Suppiah, K.; Leng, T.P.; Husseinsyah, S.; Rahman, R.; Keat, Y.C.; Heng, C.W. Thermal properties of carboxymethyl cellulose (CMC) filled halloysite nanotube (HNT) bio-nanocomposite films. *Mater. Today Proc.* **2019**, *16*, 1611–1616. [CrossRef]

75. Rana, V.K.; Pandey, A.K.; Singh, R.P.; Kumar, B.; Mishra, S.; Ha, C.-S. Enhancement of thermal stability and phase relaxation behavior of chitosan dissolved in aqueous l-lactic acid: Using 'silver nanoparticles' as nano filler. *Macromol. Res.* **2010**, *18*, 713–720. [CrossRef]

76. Werner, K.; Pommer, L.; Broström, M. Thermal decomposition of hemicelluloses. *J. Anal. Appl. Pyrolysis* **2014**, *110*, 130–137. [CrossRef]

77. Paulino, A.T.; Simionato, J.I.; Garcia, J.C.; Nozaki, J. Characterization of chitosan and chitin produced from silkworm crysalides. *Carbohydr. Polym.* **2006**, *64*, 98–103. [CrossRef]

78. Strydom, C.A.; Collins, A.C.; Bunt, J.R. The influence of various potassium compound additions on the plasticity of a high-swelling South African coal under pyrolyzing conditions. *J. Anal. Appl. Pyrolysis* **2015**, *112*, 221–229. [CrossRef]

79. Wang, K.; Du, L.; Zhang, C.; Lu, Z.; Lu, F.; Zhao, H. Preparation of chitosan/curdlan/carboxymethyl cellulose blended film and its characterization. *J. Food Sci. Technol.* **2019**, *56*, 5396–5404. [CrossRef]

80. Ferrero, F.; Periolatto, M. Antimicrobial finish of textiles by chitosan UV-curing. *J. Nanosci. Nanotechnol.* **2012**, *12*, 4803–4810. [CrossRef]

81. Hatta, F.F.; Yahya, M.Z.A.; Ali, A.M.M.; Subban, R.H.Y.; Harun, M.K.; Mohamad, A.A. Electrical conductivity studies on PVA/PVP-KOH alkaline solid polymer blend electrolyte. *Ionics* **2005**, *11*, 418–422. [CrossRef]

82. Petrowsky, M.; Frech, R. Application of the Compensated Arrhenius Formalism to Self-Diffusion: Implications for Ionic Conductivity and Dielectric Relaxation. *J. Phys. Chem. B* **2011**, *114*, 8600–8605. [CrossRef]

83. Pandey, G.P.; Agrawal, R.C.; Hashmi, S.A. Magnesium ion-conducting gel polymer electrolytes dispersed with fumed silica for rechargeable magnesium battery application. *J. Solid State Electrochem.* **2010**, *15*, 2253–2264. [CrossRef]

84. Maheshwaran, C.; Mishra, K.; Kanchan, D.K.; Kumar, D. Mg2+ conducting polymer gel electrolytes: Physical and electrochemical investigations. *Ionics* **2020**, *26*, 2969–2980. [CrossRef]

85. Rahman, N.A.; Hanifah, S.A.; Mobarak, N.N.; Ahmad, A.; Ludin, N.A.; Bella, F.; Su'Ait, M.S. Chitosan as a paradigm for biopolymer electrolytes in solid-state dye-sensitised solar cells. *Polymer* **2021**, *230*, 124092. [CrossRef]

86. Dannoun, E.M.A.; Aziz, S.B.; Brza, M.A.; Nofal, M.M.; Asnawi, A.S.F.M.; Yusof, Y.M.; Al-Zangana, S.; Hamsan, M.H.; Kadir, M.F.Z.; Woo, H.J. The Study of Plasticized Solid Polymer Blend Electrolytes Based on Natural Polymers and Their Application for Energy Storage EDLC Devices. *Polymers* **2020**, *12*, 2531. [CrossRef] [PubMed]

87. Ikram, S.; Ahmed, S.; Wazed Ali, S.; Agarwal, H. Chitosan-based polymer electrolyte membranes for fuel cell applications. *Org. Compos. Polym. Electrolyte Membr. Prep. Prop. Fuel Cell Appl.* **2017**, 381–398. [CrossRef]

88. Xu, T.; Liu, K.; Sheng, N.; Zhang, M.; Liu, W.; Liu, H.; Dai, L.; Zhang, X.; Si, C.; Du, H.; et al. Biopolymer-based hydrogel electrolytes for advanced energy storage/conversion devices: Properties, applications, and perspectives. *Energy Storage Mater.* **2022**, *48*, 244–262. [CrossRef]

89. Hung, C.-L.; Chen, M.; Sohaimy, M.I.H.; Isa, M.I.N. Proton-Conducting Biopolymer Electrolytes Based on Carboxymethyl Cellulose Doped with Ammonium Formate. *Polymers* **2022**, *14*, 3019. [CrossRef]

90. Liu, X.; Fan, X.; Liu, B.; Ding, J.; Deng, Y.; Han, X.; Zhong, C.; Hu, W. Mapping the Design of Electrolyte Materials for Electrically Rechargeable Zinc–Air Batteries. *Adv. Mater.* **2021**, *33*, 2006461. [CrossRef]

91. Munaoka, T.; Yan, X.; Lopez, J.; To, J.W.F.; Park, J.; Tok, J.B.H.; Cui, Y.; Bao, Z. Ionically Conductive Self-Healing Binder for Low Cost Si Microparticles Anodes in Li-Ion Batteries. *Adv. Energy Mater.* **2018**, *8*, 1703138. [CrossRef]

92. Cai, M.; Park, S. Spectroelectrochemical Studies on Dissolution and Passivation of Zinc Electrodes in Alkaline Solutions. *J. Electrochem. Soc.* **1996**, *143*, 2125–2131. [CrossRef]

93. Kumar, G.G.; Sampath, S. Electrochemical characterization of poly(vinylidenefluoride)-zinc triflate gel polymer electrolyte and its application in solid-state zinc batteries. *Solid State Ion.* **2003**, *160*, 289–300. [CrossRef]

94. Girish Kumar, G.; Sampath, S. Electrochemical and spectroscopic investigations of a gel polymer electrolyte of poly(methylmethacrylate) and zinc triflate. *Solid State Ion.* **2005**, *176*, 773–780. [CrossRef]

95. Tafur, J.P.; Romero, A.J.F. Interaction between Zn2+ cations and n-methyl-2-pyrrolidone in ionic liquid-based Gel Polymer Electrolytes for Zn batteries. *Electrochim. Acta* **2015**, *176*, 1447–1453. [CrossRef]

96. Béjar, J.; Álvarez-Contreras, L.; Ledesma-García, J.; Arjona, N.; Arriaga, L.G. An advanced three-dimensionally ordered macroporous NiCo$_2$O$_4$ spinel as a bifunctional electrocatalyst for rechargeable Zn–air batteries. *J. Mater. Chem. A* **2020**, *8*, 8554–8565. [CrossRef]

97. Díaz-Patiño, L.; Béjar, J.; Ortiz-Ortega, E.; Trejo, G.; Guerra-Balcázar, M.; Arjona, N.; Álvarez-Contreras, L. Zinc-Air Battery Operated with Modified-Zinc Electrodes/Gel Polymer Electrolytes. *ChemElectroChem* **2022**, *9*, e202200222. [CrossRef]

98. Wei, Y.; Wang, M.; Xu, N.; Peng, L.; Mao, J.; Gong, Q.; Qiao, J. Alkaline Exchange Polymer Membrane Electrolyte for High Performance of All-Solid-State Electrochemical Devices. *ACS Appl. Mater. Interfaces* **2018**, *10*, 29593–29598. [CrossRef]

99. Zhang, J.; Fu, J.; Song, X.; Jiang, G.; Zarrin, H.; Xu, P.; Li, K.; Yu, A.; Chen, Z. Laminated Cross-Linked Nanocellulose/Graphene Oxide Electrolyte for Flexible Rechargeable Zinc-Air Batteries. *Adv. Energy Mater.* **2016**, *6*, 1600476. [CrossRef]

100. Fan, X.; Liu, J.; Song, Z.; Han, X.; Deng, Y.; Zhong, C.; Hu, W. Porous nanocomposite gel polymer electrolyte with high ionic conductivity and superior electrolyte retention capability for long-cycle-life flexible zinc–air batteries. *Nano Energy* **2019**, *56*, 454–462. [CrossRef]

101. Li, Y.; Fan, X.; Liu, X.; Qu, S.; Liu, J.; Ding, J.; Han, X.; Deng, Y.; Hu, W.; Zhong, C. Long-battery-life flexible zinc–air battery with near-neutral polymer electrolyte and nanoporous integrated air electrode. *J. Mater. Chem. A* **2019**, *7*, 25449–25457. [CrossRef]

102. Poosapati, A.; Negrete, K.; Thorpe, M.; Hutchison, J.; Zupan, M.; Lan, Y.; Madan, D. Safe and flexible chitosan-based polymer gel as an electrolyte for use in zinc-alkaline based chemistries. *J. Appl. Polym. Sci.* **2021**, *138*, 50813. [CrossRef]

103. Song, W.; Wang, Y.; Deng, H. Ion-conducting polymer gels of polyacrylamide embedded with K$_2$CO$_3$. *J. Appl. Polym. Sci.* **2004**, *92*, 2076–2081. [CrossRef]

104. Ng, P.L.; Jamaludin, A.; Alias, Y.; Basirun, W.J.; Ahmad, Z.A.; Mohamad, A.A. Effect of KOH concentration in the gel polymer electrolyte for direct borohydride fuel cell. *J. Appl. Polym. Sci.* **2012**, *123*, 2662–2666. [CrossRef]